Biophysical Journal Volume: 00 Month Year 1–16

A Novel Engineered Membrane to Measure Electroporation: Effect of Tethers and Bioelectronic Interface

William Hoiles,[†] Charles G. Cranfield,[‡] Vikram Krishnamurthy,[†*] Bruce Cornell[§]

[†]Department of Electrical and Computer Engineering, University of British Columbia, Vancouver, Canada, V6T 1Z4; [‡] School of Medical and Molecular Biosciences, University of Technology Sydney, Broadway, NSW, Australia and the Victor Chang Cardiac Research Institute, Darlinghurst, New South Wales,; [§]Surgical Diagnostics, Roseville, New South Wales, Australia

Abstract

This paper reports on the construction and predictive models for an engineered tethered membrane. A key feature of the engineered membrane is that it provides a controllable and physiologically relevant environment for the study of the electroporation process. The mixed self-assembled membrane is formed via a rapid solvent exchange technique. The membrane is tethered to the gold electrode and includes an ionic reservoir separating the membrane and gold surface. Above the membrane there is an electrolyte solution, and a counter gold electrode. A voltage is applied between the gold electrodes and the current measured. The current is dependent on the energy required to form aqueous pores and the conductance of each pore. Modelling the membrane as a dielectric and elastic continuum, we construct a free energy model for pores in the membrane. The free energy model is constructed using the Poisson-Nernst-Planck (PNP) system of equations with an activity coefficient to model the steric effects of ions in the electrolyte. The electrical energy required to form a pore is estimated using the PNP system of equations coupled to the Maxwell stress tensor. The tethers are modelled as Hookean spring anchors to the membrane surface. The conductance of pores in the membrane are estimated using the generalized PNP equations to account for the finite size of ions, multiple ionic species, and the Stern and diffuse layers present. The population and radii of pores in the membrane are estimated using asymptotic approximations to the Smoluchowski-Einstein equation that are dependent on the energy required to form the pores. Using an equivalent circuit model of the tethered membrane, the current is predicted using the estimated pore population, radii, and the conductance of the pores, and compared with experimentally measured current for different tethering densities.

*Correspondence: vikramk@ece.ubc.ca

Introduction

Electroporation is a technique that causes the permeability of a biological membrane to increase in response to an applied electric field. The application of electrochemotherapy for antitumor treatment, protein insertion, gene and drug delivery are all of significant interest to the pharmaceutical industry (1). Over the past three decades the complex process of electroporation has been studied both experimentally and theoretically; however, the process is still poorly understood (1, 2). The electroporation process can be described as having two stages: the first is the nucleation and destruction of aqueous pores, and the second is the dynamics of formed pores. The nucleation of pores is currently an active area of research employing stochastic methods and molecular dynamics simulations (2, 3). The dynamics of created pores are governed by the free energy of the pores.

Experimental validation of theoretical models of electroporation is very difficult as the size of pores is on the nm scale and typical electroporation measurements are on the length scale of μm. Since the dynamics of pore radii can not be measured, the validation of the models is carried out using conductance measurements of the membrane. The validation of the theoretical models using synthetic bilayer lipid membranes is useful but is not a good representation of physiological systems as effects

0006-3495/08/09/2624/12 $2.00 DOI

caused by the cytoskeletal network are not present. Using cells *in vitro* provides a physiological system for validation; however, it is impossible to fully define the physiological environment which effects properties associated with electroporation. In this work, the novel engineering and predictive modelling of a tethered lipid membrane platform is presented for the study of electroporation in a physiologically relevant environment. The key feature of the engineered tethered membrane is that the experimentalist can select the desired density of tethers and membrane composition (4–7). Using the rapid solvent exchange technique to construct the membrane also reduces the defect density as compared with membranes constructed using the frequently used vesicle fusion technique allowing the engineered membrane to have a lifetime of several months (6, 8, 9).

A schematic of the *engineered tethered bilayer lipid membrane* is given in Fig. 1. The engineered tethered membrane is composed of a self-assembled monolayer of mobile lipids, and a self-assembled monolayer of tethered and mobile lipids. The tethered lipids are anchored to the gold electrode via polyethylene glycol chains. Spacer molecules are used to ensure the tethers are evenly spread over the gold electrode. The intrinsic spacing between tethers and spacers is maintained by the benzyl disulfide moieties which bond the spacers and tethers to the electrode surface. The ratio of the total number of tethers to spacers and tether molecules in the engineered tethered membrane is given by the tethering density (i.e. a 10% tether density defines that for every 9 spacer molecules there is 1 tether molecule). In the special case of 100% tethering, the engineered tethered membrane is composed of a tethered archaebacterial based monolayer with no spacer molecules. As experimentally illustrated in (8), it is not possible to construct a 0% tethered membrane as any formed membrane binds to the gold surface. As the electrolyte reservoir separating the membrane and electrode surface is required for the normal physiological function of the membrane, and noting that all prokaryotic and eukaryotic cell membranes contain cytoskeletal supports with a 1% to 10% tether density, the inability to construct a 0% tethered membrane does not inhibit the study of the electroporation process in a physiologically relevant environment. A time-dependent voltage potential is applied between the electrodes to induce a transmembrane potential of electrophysiological interest; this results in a current $I(t)$ related to the charging of the double-layers and the nucleation and destruction of aqueous pores in the engineered tethered membrane.

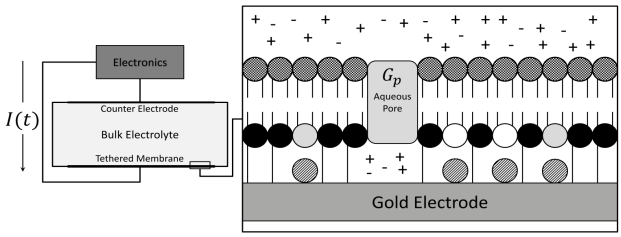

FIGURE 1: Overview of the engineered tethered membrane, model, and measured and predicted current $I(t)$. The "Electronics" block represents the electronic system which produces the drive potential between the electrode and counter electrode, and records the current response $I(t)$. The test chamber contains the synthetic tethered membrane. The tethered membrane layer is composed of the lipid components: zwitterionic C20 diphytanyl-ether-glycerophosphatidylcholine, denoted as DphPC, (grey), C20 diphytanyl-diglyceride ether (white), benzyl disulfide diphytanyl bis-tetra-ethyleneglycol (black). Spacer molecules (i.e. benzyl disulfide tetra-ethyleneglycol) are used to control the spacing between the tethered lipids (cross-hatch fill). The mobile lipid layer (square fill) is composed of the DphPC lipids. Note that for the 100% tether density the membrane is composed of a membrane spanning lipid, the structure is provided in (10), with no spacer molecules. The tethered membrane does not contain any ion channels; therefore, all current passing through the tethered membrane takes place via conducting aqueous pores with an electrical conductance denoted by G_p.

To draw quantitative conclusions about the electroporation process using the engineered tethered membrane requires a predictive model. The first models of electroporation were based on using statistical physics of stochastic processes that are dependent on the energy required to form a pore. The most widely used model for the statistics of aqueous pores formed via electroporation is the Smoluchowski-Einstein equation derived from statistical mechanics (11–13). Several models governing the pore energy have been presented in the literature (14–21). The membrane is generally modelled as a dielectric and elastic continuum (14, 22–27). Aqueous pore formation involves the creation of a hydrophilic pore, generally assumed to by a water filled cylinder with a free energy given in terms of modified Bessel's functions, which either spontaneously converts to a stable hydrophilic pore or spontaneously collapses (21, 28, 29). Although different pore shapes and corresponding pore energies can be considered for the hydrophobic pore, typically a toroidal pore is assumed (18, 20, 30). Note that the toroidal structure corresponds to the estimated hydrophilic pore shape obtained from molecular dynamics simulations (3, 31, 32). The classical free energy model for a hydrophobic aqueous pore $W(r, V_m)$ in the membrane consists of four energy terms: the pore edge

energy γ, the membrane surface tension σ, the electrostatic interaction between lipid heads, and the transmembrane potential energy contribution $W_{\rm es}(r, V_m)$. Several other contributions have been considered in the literature including effects from the cytoskeletal network (19), osmotic pressure contributions (33), electrocompressive forces (34), and bound peptides (35, 36). The classical pore energy typically used is given by (20):

$$W(r, V_m) = 2\pi\gamma r - \pi\sigma r^2 + (\frac{C}{r})^4 + W_{\rm es}(r, V_m) + W_{\rm m}, \tag{1}$$

with the energy contribution from the mechanobiological properties of the cell included as $W_{\rm m}$ (i.e. cytoskeleton). With the energy of a pore defined by Eq. 1, the key element that couples the experimental measurements with the predicted model is the aqueous pore conductance G_p (29, 30, 37–39). Discussion of G_p, $W_{\rm es}$, and $W_{\rm m}$ is provided below.

Estimates of G_p model the conduction of aqueous pores as originating from two contributions: one from the internal conductance of the pore which includes effects from steric hindrance, and the external "spreading conductance" (12, 38, 40, 41). Near the pore entrance significant nonlinear potential gradients are present which restrict the current flowing through the pore, this effect is denoted as the spreading conductance. Assuming an infinite electrolyte bath on both sides of the membrane and neglecting electrodiffusive effects, the spreading conductance for a pore of radius r and electrolyte conductivity ς_e is given by $2\varsigma_e r$, computed from the Laplace equation for electrostatics (39, 41, 42). The total pore conductance, neglecting electrodiffusive effects, is given by (12, 38, 40):

$$G_p = \frac{2\pi r^2 \varsigma_e \varsigma_p}{\pi r \varsigma_p + 2h_m \varsigma_e}, \tag{2}$$

where h_m is the membrane thickness and ς_p is the pore conductance which implicitly includes the steric effects of ions entering the pore. Recent models for computing $W_{\rm es}$ utilize the Maxwell stress tensor with the electric field computed from the solution of the Laplace equation for electrostatics (18). As we show in this paper, including electrodiffusive effects is important when estimating the pore conductance G_p and electrical energy required to form a pore $W_{\rm es}$.

The mechanobiological properties of the membrane directly effect the electroporation process, as seen in (1). Neglecting the energy contribution from the cytoskeleton network, $W_{\rm m}$, can introduce severe errors in the estimated energy (1). Experimental evidence shows that the cytoskeletal network provides a degree of mechanical integrity to the cell membrane and is therefore a vital component of the pore energy (44–50). The linkages of the cytoskeleton to the membrane are analogous to "springs" and act to restrain the enlargement of aqueous pores. Modelling the mechanical properties of the membrane as an elastic continuum and assuming a permanent cytoskeletal network anchorage, the effect of these anchors are accounted for via the energy required to deform the Hookean springs–formally, the energy contribution can be modelled using $W_m = 0.5K_{\rm cyto}r^2$ with $K_{\rm cyto}$ denoting the spring constant of the cytoskeleton network (19). The accuracy of this model for the anchoring of a membrane have not been studied quantitatively as a result of the complexities associated with the experimental measurements (46–49).

In this paper we report on the construction and predictive models of the engineered tethered membrane that includes contributions from asymmetric electrolytes, multiple ionic species, and the Stern and diffuse electrical double layers present. The models are constructed by assuming the membrane behaves as a dielectric and elastic continuum. The electrodiffusion properties of the electrolyte are modelled using a Generalized Poisson-Nernst-Planck (GPNP) system of equations with a "Langmuir type" activation coefficient (51–53). To estimate G_p, we use the GPNP in a toroidal pore geometry. Based on the GPNP and Maxwell stress tensor we construct a model for the electrical energy required to form a pore $W_{\rm es}$ that includes electrodiffusive effects. The energy required to deform the tethers is accounted for using the energy model $W_m = 0.5K_{\rm t}r^2$. Modelling the engineered tethered membrane system as an equivalent circuit model, shown in Fig. 3, and using asymptotic approximations to the Smoluchowski-Einstein equation for electroporation, we construct a predictive model for the current $I(t)$ in Fig. 1 that is dependent on the energy to form a pore W, defined in Eq. 1. Numerical results and experimental measurements with different tethering densities and lipid compositions are used to validate the accuracy of the models and exemplify the application of the engineered tethered membrane to quantify the contribution the tethers and bioelectronic interface have on the electroporation process. Specifically, we estimate the electroporation parameters of the engineered tethered membrane in Fig. 1 for the membrane tether densities of 1% and 10% for the tethered DphPC lipid bilayer, and the 100% tethered DphPC monolayer membrane.

Materials and Methods

Novel features, construction, and predictive models of the engineered tethered membrane are provided in this section. The accuracy of the models are verified using experimental measurements of the engineered tethered membrane with different tethering densities.

Formation of the Engineered Tethered Membrane

The engineered tethered membrane structure is illustrated in Fig. 1. The membrane is supported by a 25mm×75mm×1mm polycarbonate slide onto which is patterned a 100 nm sputtered gold electrode array possessing six 0.7mm×3mm active areas of membrane each of which is enclosed in a flow cell with a common gold return electrode. The formation of the tethered membrane is performed in two stages. The first stage anchors the inner layer of the membrane to the gold surface via benzyl disulphide groups. The inner layer components are introduced to the freshly deposited gold surface as ethanolic solutions of 370 μM benzyl disulphide concentrations in engineered ratios of tethers and spacers. For example the inner layer solution for the 10% tethering density is prepared by co-dissolving benzyl disulphide C20 diphytanyl bis-tetra-ethylene glycol and benzyl disulphide tetra-ethylene glycol in the ratio 1:10. The solution is exposed to the coating solution for 30 min and the electrode is then rinsed in ethanol and air dried for approximately two minutes. The coated slide is immediately assembled into a flow cell cartridge comprising six individual membranes with a common large area gold return electrode facing the membranes and separated by a 100 μm laminate defining the flow cell chamber height. The second stage of the membrane formation now occurs with the addition of 8 μL of 3 mM C20 diphytanylether lipids comprising a 70:30 mole ratio of C20 diphytanylether glycerophosphatidylcholine: C20 diphytanylether diglyceride being added to each of the flow chambers covering the membrane areas. The solution is incubated for two minutes at 20^{o}C following which, 300 μL of phosphate buffered saline was flushed through each flow cell which forms the tethered bilayer. The quality of the bilayer is measured continuously using an SDx tethered membranes tethaPodTM swept frequency impedance reader operating at frequencies of 1000, 500, 200,100,40,20,10,5,2,1,0.5,0.1 Hz and an excitation potential of 20 mV (SDx Tethered Membranes, Roseville, Sydney). The membrane was equilibrated for 30 min prior to the electroporation measurements. The electroporation measurements were performed using an eDAQ^{TM} ER466 potentiostat (eDAQ, Doig, Denistone East) and a SDx tethered membrane tethaPlate^{TM} adaptor to connect to the assembled electrode and cartridge. Individual triangular voltage ramps were applied from zero to 500 mV with a period of 2 ms. Current waveforms were recorded.

GPNP for the Electrodiffusive Behaviour in the Engineered Tethered Membrane

In this section we define the electrodiffusion model for the movement of ions in the engineered tethered membrane system illustrated in Fig. 1. The model provides the basis for computing the pore conductance G_p, and the electrical energy of an aqueous pore W_{es} in the membrane.

The ionic concentrations and electric potential dynamics in an electrolyte solution are classically modelled using the Poisson-Nernst-Planck (PNP) system of equations (54). A known weakness of the PNP model is that it does not suitably model the electrical double layers present at the membrane surface or at the electrode-electrolyte interface where Stern and diffuse charge layers are present (54). To overcome these limitations, (51) used a modified "Langmuir type" activity coefficient to account for the steric effects of ions in the electrolyte, termed the Generalized PNP (GPNP) model. The constructed GPNP model for electrodiffusion is given by (51):

$$\begin{aligned}
&\frac{\partial c^i}{\partial t} = -\nabla \cdot (J^i),\\
&J^i = -D^i \nabla c^i - F z^i q u^i_m c^i \nabla \phi\\
&\qquad\qquad - D^i c^i \nabla \ln\big(1 - \sum_{i=1}^{N} N_{\text{A}} a_i^3 c^i\big), \qquad (3a)\\
&-\nabla \cdot (\varepsilon \nabla \phi) = -\sum_i F z^i c^i. \qquad (3b)
\end{aligned}$$

In Eq. 3a, J^i is the concentration flux, c^i is the concentration, ϕ is the electrical potential, D^i is the diffusivity, N_A is Avagadro's number, a_i is the effective ion size, and u^i_m is the ionic mobility with i denoting the ionic species. In Eq. 3b, F is Faraday's constant where the superscript defines the chemical species i, q is the elementary charge, z^i is the charge valency, and ε is the electrical permittivity. The electrodiffusive model Eq. 3 is able to account for asymmetric electrolytes, multiple ionic species, and the Stern and diffuse electrical double layers present at the surface of the electrodes and membrane. Note that for $\sum_{i=1}^{N} N_{\text{A}} a_i^3 c^i \ll 1$, the steric effects are negligible in Eq. 3 and the standard PNP formulation can be used to model the electrolyte dynamics.

The membrane surface is assumed to be perfectly polarizable (i.e. blocking) such that the normal ionic flux vanishes at the surface of the membrane. There are no surface reactions present at the gold electrode to electrolyte interface; therefore, we have a no-flux boundary condition present at the gold surface. Formally these no-flux interface and boundary conditions

are given by

$$n \cdot J^i = 0 \text{ in } \partial\Omega_m \cup \partial\Omega_e \cup \partial\Omega_{ec} \tag{4}$$

with n the normal vector pointing into the electrolyte solution and J^i defined below Eq. 3. The diffusion coefficient D^i in Eq. 3a is spatially dependent as the tethering reservoir has a lower diffusion then the bulk electrolyte solution with no tethers present. We define this condition as:

$$D^i(x) = \begin{cases} D_r^i & \text{if } x \in \Omega_r \\ D_w^i & \text{if } x \in \Omega_w, \end{cases} \tag{5}$$

where Ω defines the respective domain.

The dielectric permittivity in Eq. 3b is spatially dependent as defined below:

$$\varepsilon(x) = \begin{cases} \varepsilon_w & \text{if } x \in \Omega_r \cup \Omega_w \\ \varepsilon_m & \text{if } x \in \Omega_m. \end{cases} \tag{6}$$

To ensure the well-posedness of the Poisson equation Eq. 3b, the internal boundary conditions on the membrane to electrolyte interface are satisfied by the following (55):

$$\begin{aligned} &\phi_m - \phi_w = 0 \text{ in } \partial\Omega_m, \\ &\varepsilon_m \nabla\phi_m \cdot n - \varepsilon_w \nabla\phi_w \cdot n = 0 \text{ in } \partial\Omega_m. \end{aligned} \tag{7}$$

At the electrode surface a compact Stern layer exists with a capacitance per unit are given by C_s. The Stern layer adjacent to the electrodes is modelled using the following boundary conditions

$$\begin{aligned} &C_s(\phi_e - \phi) + \varepsilon_w n \cdot \nabla\phi = 0 \text{ in } \partial\Omega_e, \\ &C_s(\phi_{ec} - \phi) + \varepsilon_w n \cdot \nabla\phi = 0 \text{ in } \partial\Omega_{ec}, \end{aligned} \tag{8}$$

with ϕ_e and ϕ_{ec} the prescribed potentials at the respective electrodes. The ambient boundary conditions of the axi-symmetric pore are given by:

$$\begin{aligned} &c^i = c_o^i \text{ in } \partial\Omega_w \cup \partial\Omega_r, \\ &n \cdot \nabla\phi = 0 \text{ in } \partial\Omega_{hm} \end{aligned} \tag{9}$$

with c_o^i the initial concentration, refer to Fig. 2.

Using equations Eq. 3, with the material properties defined by Eq. 5 and 6, and the boundary conditions Eq. 4, 7, 8, and 9, all that the remains is to define the geometry of the aqueous pores in the engineered tethered membrane.

Initially, stable pores that form in the membrane are approximately cylindrical (56). As expansion occurs, the pores become toroidal in nature. In this paper we consider the toroidal pore structure illustrated in Fig. 2 to compute the conductance of a pore. The current travelling through the pore is computed using:

$$I_p = F \sum_i \int_0^r J^i 2\pi r dr, \qquad G_p = \frac{I_p}{V_m}, \tag{10}$$

where J^i and V_m are computed using Eq. 3 with the geometry given in Fig. 2.

To compare the numerical accuracy of the GPNP model with the previously developed model in (39), we assume electroneutrality (i.e. $\sum_i z^i c^i = 0$) and no steric effects $a_i = 0$ (39). The governing equations of ϕ_w, the electrical potential in the electrolyte solution Ω_w, in the limit of electroneutrality and no steric effects, can be derived by substituting the time derivative of Eq. 3b into Eq. 3a for charge neutrality resulting in the elliptic equation:

$$\begin{aligned} &\nabla \cdot (\varsigma \nabla\phi + \nabla\kappa) = 0 \\ &\varsigma = \sum_{i=1}^N \frac{(qz^i)^2 D^i}{k_B T} c^i, \qquad \kappa = \sum_{i=1}^N q z^i D^i c^i. \end{aligned} \tag{11}$$

with the parameters defined below Eq. 3. The boundary conditions of Eq. 11 at the electrode surfaces $\partial\Omega_e$ and $\partial\Omega_{ce}$, and at the ambient boundary $\partial\Omega_w$, $\partial\Omega_{hm}$, and $\partial\Omega_r$ are given by Eq. 8 and 9 respectively, refer to Fig. 2. In the membrane domain Ω_m

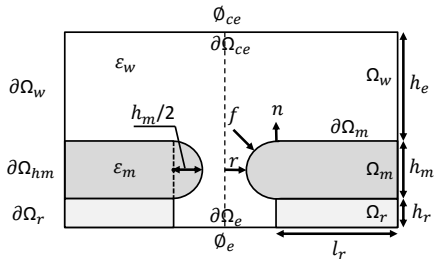

FIGURE 2: The aqueous pore is modelled as axisymmetric with dimensions given by r, l_r, h_r, h_m, and h_e for the cylindrical and toroidal geometries. The tethered membrane platform is modelled with three distinct regions: the electrolyte solution Ω_w, the electrolyte reservoir Ω_r, and the membrane Ω_m. The electrode to electrolyte interface is denoted by $\partial\Omega_e$ and $\partial\Omega_{ec}$ for the electrode and counter electrode respectively. $\partial\Omega_m$ denotes the interface between the membrane and electrolyte solution. The boundary conditions $\partial\Omega_w$ and $\partial\Omega_r$ define the ambient conditions of the electrolyte and membrane. The potentials at each electrode are defined by ϕ_e and ϕ_{ec} respectively. The electrolyte has an electrical permittivity ε_w and the membrane an electrical permittivity ε_m. The electrical force acting on the membrane is denoted by f and is defined in (15). n is the normal vector pointing from the membrane domain to the electrolyte domain.

the electrostatic potential ϕ_m is governed by Laplace's equation for electrostatics $\nabla \cdot (\varepsilon_m \nabla\phi) = 0$. The interface conditions between the domains Ω_w and Ω_m are given by:

$$\begin{aligned} &n \cdot \nabla\phi_w = 0 \text{ in } \partial\Omega_m, \\ &\phi_m = \phi_w \text{ in } \partial\Omega_m. \end{aligned} \tag{12}$$

From the continuity of potential on $\partial\Omega_m$ Eq. 12, there exists a surface charge on the membrane given by $\rho_s = \varepsilon_m n \cdot \nabla\phi_m - \varepsilon_w n \cdot \nabla\phi_w$; therefore, the system of equations Eq. 11 with boundary conditions Eq. 12 implicitly includes the membrane surface charge ρ_s (18, 39, 57).

We denote the governing equations Eq. 3a with $a_i = 0$ coupled with Eq. 11, the materials defined by Eq. 5 and 6 and the boundary conditions Eq. 4, 8, 9, and 12 as the *Electroneutral Model* (EM). Given the solution of the EM system of equations, the conductance G_p, Eq. 10, can be estimated assuming negligible steric effects and electroneutrality.

Electrical Energy Required to Form a Pore

In this section we construct a model for the electrical energy of a pore, W_{es}, in the engineered tethered membrane by modelling the membrane as a dielectric continuum in an electrolyte solution. The computation of W_{es} involves computing the force that causes a displacement of the pore structure. Consider the pore structure presented in Fig. 2. The pore boundary is assumed to only expand in the radial direction r. If we denote $F(r)$ as the total force acting on the pore boundary of radius r, then the electromechanical energy can be computed using (18, 43, 58):

$$W_{\text{es}}(r) = -\int_0^r F(r)dr. \tag{13}$$

Using the Maxwell stress tensor we show how $F(r)$ can be computed for the pore structures in Fig. 2.

The electric field induces a stress on the membrane surface. The total stress on the surface of the membrane can be computed using the Maxwell stress tensor T given by (18, 43, 59–65):

$$T = \varepsilon(\frac{1}{2}|\nabla\phi|^2 I - \nabla\phi \otimes \nabla\phi), \tag{14}$$

where ε and ϕ are defined below Eq. 3, I denotes the identity matrix, and $\otimes$ is the dyadic product. The stress on the membrane from the electrolyte p_w, and the stress on the electrolyte from the membrane p_m are given by:

$$\begin{aligned} p_w &= -T_w n = -\varepsilon_w(\frac{1}{2}|\nabla\phi_w|^2 I - \nabla\phi_w \otimes \nabla\phi_w)n, \\ p_m &= T_m n + f \\ &= -\varepsilon_m(\frac{1}{2}|\nabla\phi_m|^2 I - \nabla\phi_m \otimes \nabla\phi_m)n + f, \end{aligned} \tag{15}$$

where f is the stress induced from all other elastic properties of the membrane (66–68). Note that f denotes the electrical force density acting on the membrane surface.

The membrane is assumed to be at local mechanical equilibrium at the pore surface such that $f = (T_w - T_m)n$. Therefore, to maintain local equilibrium the total force acting on the pore boundary $F(r)$ is given by:

$$F(r) = \int_S n \cdot (p_w - p_m) dS, \tag{16}$$

with p_w and p_m defined in Eq. 15, and the surface S and normal vector n given in Fig. 2. Given ϕ computed using Eq. 3, we can compute $F(r)$ using Eq. 16. Substituting $F(r)$ into Eq. 13 gives the electrical energy contribution to pore formation in the membrane. Note that $F(r)$ includes electrical double layer and electrodiffusive effects caused by asymmetric electrolytes.

Note that for narrow cylindrical pores $\partial\phi/\partial r \approx 0$ and $\partial\phi/\partial z \approx V_m/h_m$ on S; substituting into Eq. 15 and 16 we see that $F(r, V_m) \propto V_m^2$ with V_m the transmembrane potential. The proportionality of $F(r, V_m) \propto V_m^2$, whch also implies $W_{\text{es}}(r, V_m) \propto V_m^2$, is critical for the derivation of the electrical energy required to form a pore in (18, 28, 40). This allow the computation of $F(r, V_m)$ to be conducted using a single instance of $F(r)$ for a given transmembrane potential V_m which is used to estimate the proportionality constant.

For numerical comparison to previously published results (18), we estimate the pore energy W_{es}, Eq. 13, assuming electroneutrality, negligible steric effects, and steady-state current (i.e. $\nabla c^i = 0$). With these assumptions the electrical potential ϕ is governed by Laplace's equation $\nabla \cdot (\varepsilon \nabla\phi) = 0$ with ε defined by Eq. 6, and the interface and boundary conditions defined by Eq. 8, 9, and 12. We denote this as the *Laplace Model* (LM).

Equivalent Circuit Electroporation Model of the Engineered Tethered Membrane

The electrophysiological properties of the engineered tethered membrane are modelled using an equivalent circuit model (5, 8, 10, 69, 70). Note that for a sufficiently low applied potential (i.e. less then 50 mV) the effects of electroporation are negligible. This allows the circuit parameters to be estimated with a sinusoidal excitation potential with magnitude less then 50 mV.

The tethered membrane platform is composed of three distinct regions: the electrical double layers at the gold electrodes, the bulk electrolyte reservoir, and the tethered membrane. The bulk electrolyte solution is modelled as completely ohmic with resistance R_e. The electrical double-layers contain a tightly bound region of ions on the order of an atomic radii, and a diffuse region of length on the order of the Debye-Hückel thickness. The Stern layer and diffuse charge layers are modelled using an overall capacitance C_{tdl}, and C_{bdl} for the counter electrode and electrode respectively. The tethered membrane is modelled as a uniformly polarized structure such that the charging dynamics of the membrane are represented by a capacitance C_m. The tethered membrane conductance $G_m(t, V_m)$ is both time and membrane voltage dependent with V_m denoting the transmembrane potential. The dependency of G_m is a result of the process of electroporation that takes place to generate/destroy aqueous pores in the membrane. The excitation potential $V_s(t)$ applied across the two electrodes closes the circuit. The equivalent circuit model of the tethered membrane platform is given in Fig. 3.

The governing equations of the tethered membrane system are given by:

$$\begin{aligned} \frac{dV_m}{dt} &= -(\frac{1}{C_m R_e} + \frac{G_m}{C_m})V_m - \frac{1}{C_m R_e}V_{dl} + \frac{1}{C_m R_e}V_s, \\ \frac{dV_{dl}}{dt} &= -\frac{1}{C_{dl} R_e}V_m - \frac{1}{C_{dl} R_e}V_{dl} + \frac{1}{C_{dl} R_e}V_s, \\ I &= \frac{1}{R_e}\big(V_s - V_m - V_{dl}\big), \end{aligned} \tag{17}$$

where C_{dl} is the total capacitance of C_{tdl} and C_{bdl} in series. Given $V_s(t)$, and the static circuit parameters $C_{tdl}, C_{bdl}, R_e, C_m$, and the membrane conductance G_m can be estimated from the measured current $I(t)$. However, for drive potentials below

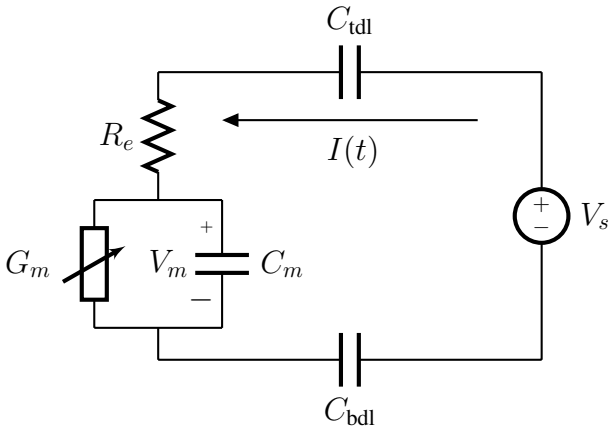

FIGURE 3: Schematic of the lumped circuit model with R_e the electrolyte resistivity, C_m is the membrane capacitance, G_m is the membrane conductance, C_{bdl} is the electrode capacitance, C_{tdl} is the counter electrode capacitance, and V_m is the transmembrane potential.

approximately 50 mV, the membrane conductance is approximately constant and is assumed at its equilibrium value G_o such that $G_m(t, V_m) \approx G_o$.

How can we experimentally verify that the formed membrane does not contain significant defects? Possible membrane defects include patches with the gold electrode directly exposed to the bulk electrolyte, or with portions of bilayer sandwiched together. Using the measured current response resulting from an excitation potential below 50 mV, we can compute the mean squared error (MSE) between the predicted current from Eq. 17 and the experimentally measured current. If a significant MSE is obtained then the model of a homogeneous membrane Eq. 17 is not suitable and the membrane is concluded to contain inhomogeneities (i.e. defects). A major concern when performing electroporation experiments is the detection of the catastrophic voltage breakdown of the membrane causing separated areas of membrane to degrade. This effect can be detected by a high MSE and a significant increase in the estimated membrane conductance C_m resulting from the electrode surface capacitance coming into contact with the bulk electrolyte. Typical values for membrane capacitance and conductance are 0.5-1.3 μF/cm^2 and 0.5-2.0 μS for an intact 1%-100% tethered membrane with surface area 2.1 mm^2.

For transmembrane potentials above 50 mV, the TMP conductance G_m can be estimated by

$$\begin{aligned} G_m &= \sum_{i=1}^{\lfloor N(t) \rfloor} G_p(r_i), \\ \frac{dr_i}{dt} &= -\frac{D}{k_B T}\frac{\partial W(r)}{\partial r_i} \quad \text{for} \quad r_i \in \{1, 2, \ldots, \lfloor N(t) \rfloor\}, \\ \frac{dN}{dt} &= \alpha e^{(\frac{V_m}{V_{ep}})^2}\big(1 - \frac{N}{N_o} e^{-q(\frac{V_m}{V_{ep}})^2}\big). \end{aligned} \tag{18}$$

In Eq. 18, α is the pore creation rate coefficient, V_{ep} is the characteristic voltage of electroporation, N_o is the equilibrium pore density at $V_m = 0$, and $q = (r_m/r_*)^2$ is the squared ratio of the minimum energy radius r_m at $V_m = 0$ with r_* the minimum energy radius of hydrophilic pores (56, 71–73). The parameters α, V_{ep}, N_o, and γ are estimated by fitting the measured current response I to the predicted current response from Eq. 17 and Eq. 18 given the drive voltage V_s.

The derivation of Eq. 18 is based on making physiologically relevant approximations to the Smoluchowski-Einstein equation for electroporation. The Smoluchowski-Einstein equation governs the distribution of pores as a function of their radius r and time t (11–13). If we denote $n(r, t)$ as the pore density distribution function, then the Smoluchowski-Einstein equation is given by:

$$\frac{\partial n}{\partial t} = D\frac{\partial}{\partial r}\Big[\frac{n}{k_B T}\frac{\partial W}{\partial r} + \frac{\partial n}{\partial r}\Big] + S(r), \tag{19}$$

where D is the diffusion coefficient of pores, k_B is the Boltzmann constant, T is the temperature, W is the pore energy, and $S(r)$ models the creation and destruction rate of pores. Making the physiologically relevant assumption that diffusion term in

Eq. 19 is negligible, and the characteristic time scale of W is longer then 0.1 μs, then the process of electroporation can be modelled by Eq. 18. Note that Eq. 18 has been used by several authors for modelling DNA translocation into cells (56, 71–75).

Numerical Methods

The governing equations Eq. 3 with boundary conditions Eq. 4, and 7-9 are solved numerically with the commercially available finite element solver COMSOL 4.3a (Comsol Multiphysics, Burlington, MA). To solve the GPNP and PNP models the COMSOL modules *Transport of Diluted Species* and *Electrostatics* are utilized; and to solve the EM model the modules *Nernst-Planck* and *Electrostatics* are utilized. Eq.(10) is used to compute the pore conductance with the integration done in the region defined in Fig. 2. The simulation domain is meshed with approximately 270,000 triangular elements constructed using an advancing front meshing algorithm. The GPNP and PNP are numerically solved using the *multifrontal massively parallel sparse direct solver* (76) with a variable-order variable-step-size backward differential formula (77). The conductance is computed for a finite number of equally spaced radii between 0.5-10 nm with a step-size of 0.25 nm. The steady-state conductance G_p, Eq. 10, is estimated when the percentage change in conductance between successive steps (i.e. $|(G_p(t_{i+1}) - G_p(t_i))/G_p(t_i)|$) is less then 1%. The total force acting on the toroidal pore $F(r)$, Eq. 16, is computed using the results from the conductance computation. Substituting $F(r)$ into Eq. 13, the total electrical energy required to form the pore W_{es} is computed. The numerical estimate of $I(t)$ is computed using Eq. 17 and 18 assuming there are a finite number of possible pore radii using the algorithm presented in (56, 71).

Results and Discussion

In this section we apply the electroporation model for the engineered tethered membrane. The predictive accuracy of the electroporation model is verified using experimental measurements of tethered DphPC membranes with a tethering density of 1%, 10%, and 100%.

Numerically Predicted Aqueous Pore Conductance and Electrical Energy Required to form a Pore

To estimate the conductance G_p, Eq. 10, and the electrical energy required to form a pore W_{es}, Eq. 13, we utilize the GPNP, Eq. 3, PNP, EM, and LM models defined in the Materials and Methods section.

In Fig. 4 the estimated pore conductance computed using the GPNP, PNP, and EM models is presented. As seen the pore conductance numerically predicted using the GPNP follows a $G_p \propto r$ relationship. For membranes with sufficiently large electrolyte baths and pore radii (i.e. electrolyte bath is hundreds of nm thick and $r > t_m$), the pore conductance follows $G_p \propto r$ (12, 38–40), in agreement with the spreading conductance derived from Laplace's equation in (42, 78). Note that the effect $G_p \propto r$ for $r < t_m$ and $h_r = 4$ nm is only numerically predicted when the effects caused by asymmetric electrolytes, finite ion size, and Stern and diffuse layers are accounted for. In Fig. 4 *A*, the GPNP and PNP models produce differing conductance estimates as a result of the steric effects present. Recall that for $\sum_{i=1}^{N} N_{\text{A}} a_i^3 c^i \ll 1$ the steric effects are negligible and the estimated conductance using the GPNP and PNP models would be identical. As seen by comparing the estimated conductance G_p in Fig. 4 *A*, the assumption of electroneutrality causes a noticeable decrease in the computed conductance G_p. As discussed in the Introduction the pore conductance G_p may be dominated by the spreading conductance, which follows a $G_p \propto r$ proportionality, when the electrolyte solution is sufficiently geometrically constrained. From Fig. 2, the tethering reservoir is $h_r = 4$ nm, and from Fig. 4 *A* we see that $G_p \propto r$; therefore, we conclude that the conductance of an aqueous pore in the engineered tethered membrane is dominated by the spreading conductance. As the diffusivity in the tethering reservoir, D_r, decreases the pore conductance decreases, as seen in Fig. 4 *B*. This is expected as less ions can flow through the pore as a result of reduced ion mobility.

Fig. 5 compares the numerically estimated electrical energy required to form a pore computed using the GPNP, PNP, EM, and LM defined in the Materials and Methods section. For small pores below 1 nm all the models provide similar estimated for W_{es}, as seen in Fig. 5 *A*. The PNP and EM models provide a significantly lower estimate of W_{es} compared to the GPNP and LM models for large pore radii above 4 nm. The discrepancy between the estimated W_{es} is a result of the assumption of negligible steric effects in the PNP model, and the assumption of negligible steric effects and electroneutrality in the EM model. Note that although the GPNP and LM models provide similar predictions of W_{es}, the LM assumes negligible steric effects, electroneutrality, and steady-state current (i.e. $\nabla c^i = 0$) which results in the estimated voltage distribution on the surface of the membrane to differ with the voltage distribution predicted from the GPNP. Qualitatively at the surface of the membrane the GPNP model has the interface condition Eq. 7 such that $\varepsilon_m \nabla \phi_m \cdot n = \varepsilon_w \nabla \phi_w \cdot n$; however, the interface condition for the LM model Eq. 12 causes $\varepsilon_m \nabla \phi_m \cdot n \neq \varepsilon_w \nabla \phi_w \cdot n$ on the surface. This results in the LM overestimating

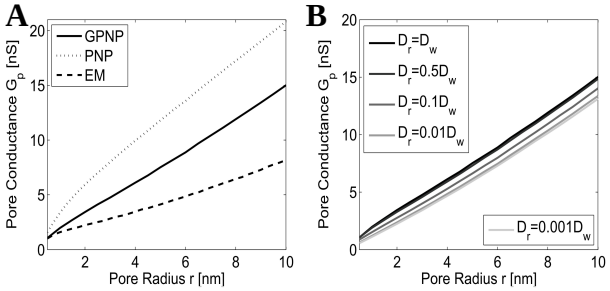

FIGURE 4: Numerically predicted pore conductance G_p, defined in Eq. 10. (*A*) provides the predicted pore conductance G_p computed using the GPNP, PNP, and EM models. (*B*) is the predicted G_p for different tethering reservoir diffusivities. The geometry of the pore is given in Fig. 2 with the parameters of the governing equations and boundary conditions provided in Table S1 in the Supporting Material.

the voltage potential when compared with the GPNP. From Eq. 15, the overestimated potential causes the computed W_{es} to be larger when using the LM model as compared with the GPNP model. As discussed, the assumption of $W_{\text{es}}(r, V_m) \propto V_m^2$ is typically invoked to simplify the computation of $W_{\text{es}}(r, V_m)$ (18, 28, 40). From Fig. 5 *B*, we compute $W_{\text{es}}(r, V_m)$ explicitly for several transmembrane potentials and find that the proportionality follows a fractional power law. This illustrates the importance of including effects caused be electrodiffusion. As illustrated in Fig. 5 *C*, reducing the diffusion coefficient in the tethering reservoir D_r causes a slight reduction in the estimated W_{es}. In comparing Fig. 5 *B* with Fig. 5 *C*, the main contribution to the change in W_{es} results from a change in transmembrane potential.

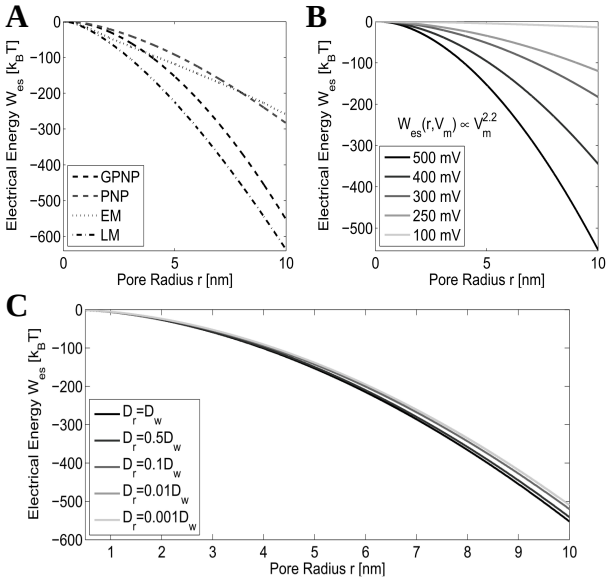

FIGURE 5: Numerically predicted electrical energy W_{es}, Eq. 13, required to form an aqueous pore. (*A*) compares the predicted W_{es} computed using the GPNP, PNP, EM, and LM models defined in the Materials and Methods section for the transmembrane potential of $V_m = 500$ mV. (*B*) presents estimates of W_{es} computed using the GPNP for the transmembrane potentials listed. (*C*) provides estimates of W_{es} computed using the GPNP for $V_m = 500$ mV for different tether reservoir diffusivities. The parameters of the governing equations and boundary conditions can be found in Table S1.

Experimental Verification of Predictive Models

In this section we use the numerically predicted pore conductance G_p, Eq. 10, and electrical energy W_{es}, Eq. 13, estimated using the GPNP model with the electroporation model given by Eq. 17 and 18 to predict the current response of the engineered

tethered membrane. The predicted current response is compared to experimentally measured data to validate the accuracy of the model. Note that all electroporation processes were reversible and did not cause permanent damage to the membrane.

From Eq. 17 and 18, if the drive potential V_s is applied and the resulting current is I_s; then if the drive potential $-V_s$ is applied the resulting current must be $-I_s$ if only the process of electroporation is present. For all the tethering densities and membrane compositions tested this relation was observed in all experimental current measurements and therefore we concluded that the only process present is that of electroporation. The drive potential $V_s(t)$ used to produce the results in Fig. 6 and 7 is defined by a linearly increasing potential of 100 V/s for 5 ms proceeded by a linearly decreasing potential of -100 V/s for 5ms.

The experimental measurement and predicted voltages, pore radii, membrane resistance, and current are presented in Fig.6 for the 10% tethered DphPC bilayer membrane. From Fig. 6 *A*, the experimentally measured and numerically predicted current are in excellent agreement. As seen in Fig. 6 *B*, the application of the voltage excitation immediately causes an increase in the double-layer voltage V_{dl} as a result of the charge increase in the charge distribution at the electrode surface. The transmembrane potential V_m simultaneously increases as a result of the excitation potential. The increase in V_m results in the formation of pores. As seen in Fig. 6 *C*, a dramatic change in the resistance results after the application of the drive potential. In Fig. 6 *D* the maximum radius $r_{\max}$ and mean radius $\bar{r}$ are provided to illustrate the spread in pore radii. As V_m increases, pores are generated and expand according to Eq. 18. From Eq. 18, all pores diffuse to the minimum-energy pore radius given by $\partial W/\partial r_i = 0$ with an advection velocity proportional to D/k_BT. As seen in Fig. 6 *D*, generated pores rapidly expand to the minimum-energy pore radius as the spread between $r_{\max}$ and $\bar{r}$ is negligible.

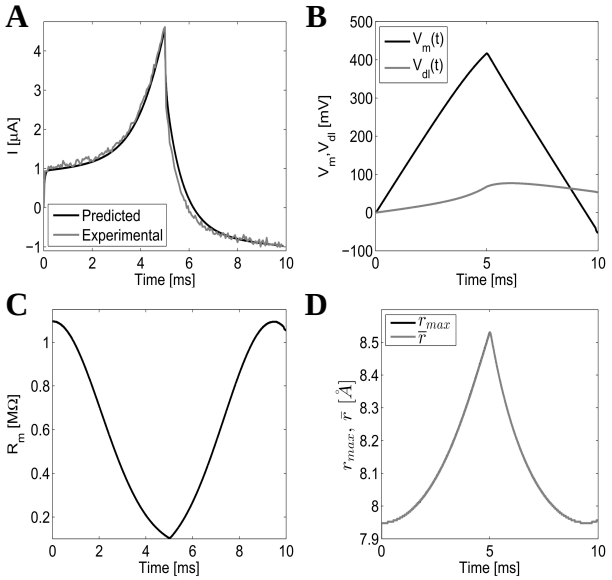

FIGURE 6: The measured and predicted current, voltage potentials, membrane resistance, and pore radii for the drive potential $V_s(t)$, defined at the beginning of this section, for the 10% tether density DphPC bilayer membrane. (*A*) is the measured and predicted current, (*B*) the predicted transmembrane V_m and double-layer potential V_{dl} defined in Eq. 17, (*C*) is the estimated membrane resistance, and (*D*) the estimated maximum $r_{\max}$ radius, and mean pore radius $\bar{r}$. All predictions are computed using Eq. 17 and Eq. 18 with the parameters defined in Table S2 of the Supporting Material.

As seen from Fig.6 the predictive model is able to estimate the current response of the engineered tethered membrane; however an immediate question arises: how sensitive is the predicted current response to errors in the model parameters of Eq. 17 and Eq. 18? To reduce the number of free parameters we set γ, σ, C, D to the experimentally measured values given in (13, 20, 29, 34, 56, 71). The estimated values of G_o, C_m, C_{dl}, and R_e are provided in Table S2 of the Supporting Material and correspond to a homogeneous membrane with negligible defects, as discussed in the Materials and Methods section. Note that all errors in Table S2 are estimated by computing the range of values in good agreement with the experimentally measured current using Eq. 17 and Eq. 18. As seen, the electrolyte resistance R_e has a negligible effect on the current response as the membrane conductance and capacitive charging dominate the current flow. Using a triangular drive potential allows the estimate of C_m, R_m, and C_{dl} using specific sections of the measured current. The initial jump in current at the start of the triangular pulse is dominated by C_m. The current response proceeding the initial jump is dominated by G_o with the slope

proportional to the membrane conductance G_o. Note that any deviation from a linear current response in this region is a result of the electroporation process. The double layer capacitance C_{dl} effect dominates the current response as the triangular drive potential decreases. By estimating each of the circuit parameters using specific regions of the current response allows the circuit parameters to be reliably estimated, as seen in Table S2. The pore creation rate Eq. 18 is not significantly effected by α and N_o because dN/dt is exponentially dependent on V_m, V_{ep}, and q. This dependence can be seen by referring to Table S2 where the estimated error of α and N_o is significantly larger then V_{ep} and q. The estimated values for N_o, α, Vep, q are in excellent agreement with experimentally estimated values found in the literature (29, 74, 79).

Fig. 7 provides the experimental current measurement and the predicted current and membrane resistance $R_m = 1/G_m$ for the 1% and 10% DphPC bilayer, and the 100% DphPC monolayer membrane. In comparing the resulting current between the 1%, 10%, and 100% tethered case, Fig. 7 *A*, we see that as the tethering density increases the effects of electroporation decreases. This is an expected result as the tethers provide structural support hindering the nucleation of pores reducing the equilibrium pore density N_o and increasing the characteristic voltage of electroporation V_{ep}. As seen in Fig. 7 *B*, the resistance begins to change at approximately 1 ms when the transmembrane potential reaches a sufficiently high to cause the nucleation of pores. The estimated spring constant K_t for the 1%, 10%, and 100% tethering density are: 0 mN/m, 2$\pm$0.5 mN/m, and 20$\pm$4 mN/m. For the 1% tether density the spring constant is negligible as expected. For the 100% tethering case pores can not expand as a result of the spring constant K_t, therefore the decrease in resistance is primarily a result of pore nucleation and destruction governed by Eq. 18. For the 100% tether density membrane, it may be the case that all pores in the membrane are hydrophilic as the tethers may prevent the transition from the hydrophilic to hydrophobic structure. If only hydrophilic pores are present, the membrane resistance would be dominated by the nucleation of pores and not the dynamics of the pores. Note that the molecular structure of the aqueous pores can not be reliably inferred using continuum theory models and would require the use of molecular dynamics or similar non-continuum models. Interestingly, for the 1% membrane structures the resistance begins to decrease at 9.2 ms, and for the 10% membrane at 9.4 ms after the initial application of the drive potential $V_s(t)$ defined at the beginning of this section. This is a result of the charge accumulation in the electrical double layers at the gold electrode surface, V_{dl}, discharging causing an increase in the magnitude of the transmembrane potential V_m. This illustrates the importance of including electrical double-layer effects when modelling gold electrodes. Note that when using Eq. 17 and Eq. 18 for estimating the effects of electroporation for rapidly changing drive potentials, the double-layer capacitance in Eq. 17 can become time dependent (51). In such cases the dynamics of the time dependent capacitance can be estimated using the GPNP model defined in Eq. 3 using the method outlined in (51) with the electroporation model developed in this paper. The thickness of the membrane can be estimated using $h_m = \varepsilon_m A_m / C_m$ with $A_m = 1.2$ mm^2, the area of the membrane surface, and ε_m and C_m given in Table S1 and S2 in the Supporting Material. For the 1%, 10%, and 100% membranes we obtain a thickness of: 3.54 nm, 3.54 nm, 3.40 nm. These values are in excellent agreement with NMR measurement of similar DphPC based tethered membranes (8). As seen, the thickness of the tethered DphPC membrane is approximately constant between the 1% and 10% tether densities. The 100% DphPC monolayer is slightly thinner then the 1% and 10% DphPC bilayer membrane. The reduction in thickness between the 100%, and the 1% and 10% is a result of the combined effect of an increased tether density and the dibenzyl group that binds the phytanyl tails in the tethered DphPC monolayer.

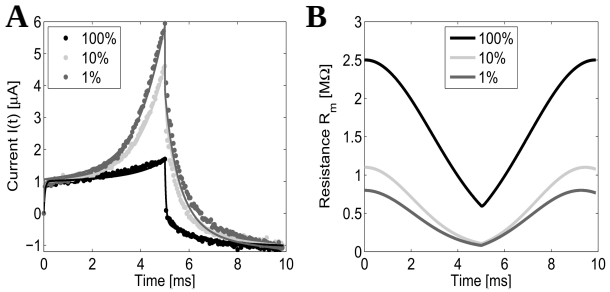

FIGURE 7: Experimentally measured and numerically predicted current $I(t)$ (*A*), and membrane resistance $R_m = 1/G_m$ (*B*) for the drive potential $V_s(t)$ defined at the beginning of this section. The tethering densities 1% and 10% correspond to the DphPC bilayer and the 100% corresponds to the DphPC monolayer. All predictions are computed using Eq. 17 and Eq. 18 with the parameters defined in Table S2.

In Fig.8 the experimentally measured and numerically predicted current $I(t)$ is provided for several different linearly increasing and decreasing drive potentials. As seen from Fig.8 *A-D*, we obtain excellent agreement between the experimentally measured and numerically predicted current. For small magnitude drive potentials one would expect the membrane

resistance to remain constant as the effects of electroporation, governed by Eq. 17 and Eq. 18, are negligible. Indeed from Fig.8 *A* and *D*, we see that the electroporation effects are negligible for drive potentials from 50 to 80 V/s for the 1 ms rise, and 10-40 V/s for the 5 ms rise. The reason the 5 ms rise, Fig.8 *A* and *C*, has larger relative electroporation effects as compared with the 1 ms rise, Fig.8 *B* and *D*, is that the nucleation and dynamics of pore radii evolve for a longer period of time at a sufficiently high transmembrane potential. As expected, the magnitude of the current response for the 10% tethered membrane, Fig.8 *A* and *B*, is less then the current response for the 10% tethered membrane, Fig.8 *C* and *D*, as a result of the tethers hindering the nucleation and expansion of pores. The estimated electrical double-layer capacitance used to compute the current for the 10% membrane is $C_{dl} = 65$ nF, and that for the 1% tether density is $C_{dl} = 39$ nF. In reference to Table S3 of the Supporting Material, the expected value of $C_{dl} \in [118, 137]$ nF. Despite this minor discrepancy, the estimated current, using the model given in Eq. 17 and Eq. 18, is in excellent agreement with the experimentally measured current.

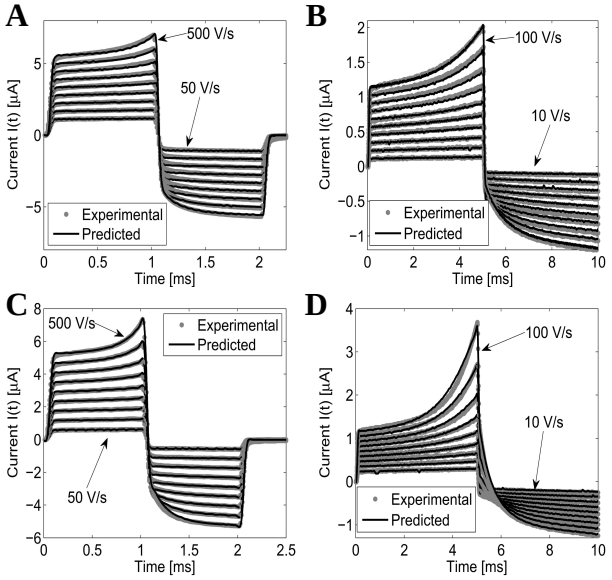

FIGURE 8: Experimentally measured and numerically predicted current response $I(t)$ for the 10% tethering density DphPC membrane, panels (*A*) and (*B*), and the 1% tether density DphPC membrane, panels (*C*) and (*D*). In panels (*A*) and (*C*), the drive potential $V_s(t)$ is defined by a 1 ms linearly increasing with a rise time of 50 to 500 V/s in steps of 50 V/s proceeded by a linearly decreasing potential of -50 to -500 V/s in steps of -50 V/s for 1 ms. In panels (*B*) and (*D*), the drive potential $V_s(t)$ is defined by a 5 ms linearly increasing potential for 10 to 100 V/s in steps of 10 V/s proceeded by a linearly decreasing potential of -10 to -100 V/s in steps of -10 V/s for 5 ms. The numerical predictions are computed using Eq. 17 and Eq. 18 with the parameters defined in Table S3 of the Supporting Material.

Conclusion

The construction and predictive models for an engineered tethered membrane is presented in this paper. The self-assembled membrane can be setup with ease and provides a physiologically relevant environment for the study of electroporation. The analysis presented reveals several interesting features regarding how the Stern and diffuse double-layers, and tethers effect the electroporation process. Numerically we found that the electrical energy required to form a pore has the property that $W_{\text{es}}(r, V_m) \propto V_m^{2.2}$ and that the pore conductance has the property $G_p \propto r$, where V_m is the transmembrane potential and r is the radius of the pore. As shown, the experimental results compare favourably with the results computed from the predictive models.

SUPPORTING MATERIAL

Tables S1, S2, and S3 are available at www.biophys.org/biophysj/supplemental/S0006-3495(XX)XXXXX-X.

References

[1] Kee, S., J. Gehl, and E. Lee, 2011. Clinical aspects of electroporation. Springer.
[2] Kotulska, M., 2007. Natural fluctuations of an electropore show fractional Lévy stable motion. Biophysical journal 92:2412–2421.
[3] Böckmann, R., B. Groot, S. Kakorin, E. Neumann, and H. Grubmüller, 2008. Kinetics, statistics, and energetics of lipid membrane electroporation studied by molecular dynamics simulations. Biophysical journal 95:1837–1850.
[4] Cornell, B., V. Braach-Maksvytis, L. King, P. Osman, B. Raguse, L. Wieczorek, and R. Pace, 1997. A biosensor that uses ion-channel switches. Nature 387:580–583.
[5] Raguse, B., V. Braach-Maksvytis, B. Cornell, L. King, P. Osman, R. Pace, and L. Wieczorek, 1998. Tethered lipid bilayer membranes: Formation and ionic reservoir characterization. Langmuir 14:648–659.
[6] McGillivray, D., G. Valincius, D. Vanderah, W. Febo-Ayala, J. Woodward, F. Heinrich, J. Kasianowicz, and M. Lscheb, 2007. Molecular-scale structural and functional characterization of sparsely tethered bilayer lipid membranes. Biointerphases 2:21–33.
[7] Prashar, J., P. Sharp, M. Scarffe, and B. Cornell, 2007. Making lipid membranes even tougher. Journal of Materials Research 22:2189–2194.
[8] Heinrich, F., T. Ng, D. Vanderah, P. Shekhar, M. Mihailescu, H. Nanda, and M. Losche, 2009. A new lipid anchor for sparsely tethered bilayer lipid membranes. Langmuir 25:4219–4229.
[9] Cranfield, C., B. Cornell, S. Grage, P. Duckworth, S. Carne, A. Ulrich, and B. Martinac, 2014. Transient potential gradients and impedance measures of tethered bilayer lipid membranes: pore-forming peptide insertion and the effect of electroporation. Biophysical journal 106:182–189.
[10] Krishna, G., J. Schulte, B. Cornell, R. Pace, and P. Osman, 2003. Tethered bilayer membranes containing ionic reservoirs: selectivity and conductance. Langmuir 19:2294–2305.
[11] Pastushenko, V., Y. Chizmadzhev, and V. Arakelyan, 1979. Electric breakdown of bilayer lipid membranes: II. Calculation of the membrane lifetime in the steady-state diffusion approximation. Journal of Electroanalytical Chemistry and Interfacial Electrochemistry 104:53 – 62.
[12] Barnett, A., and J. Weaver, 1991. Electroporation: a unified, quantitative theory of reversible electrical breakdown and mechanical rupture in artificial planar bilayer membranes. Bioelectrochemistry and bioenergetics 25:163–182.
[13] Freeman, S., M. Wang, and J. Weaver, 1994. Theory of electroporation of planar bilayer membranes: predictions of the aqueous area, change in capacitance, and pore-pore separation. Biophysical Journal 67:42–56.
[14] Deng, P., Y. Lee, R. Lin, and T. Zhang, 2012. Nonlinear electro-mechanobiological behavior of cell membrane during electroporation. Applied Physics Letters 101:053702.
[15] Talele, S., P. Gaynor, M. Cree, and J. Ekeran, 2010. Modelling single cell electroporation with bipolar pulse parameters and dynamic pore radii. Journal of Electrostatics 68:261 – 274.
[16] Joshi, R., Q. Hu, K. Schoenbach, and H. Hjalmarson, 2002. Improved energy model for membrane electroporation in biological cells subjected to electrical pulses. Physical Review E 65:041920.
[17] Joshi, R., and K. Schoenbach, 2000. Electroporation dynamics in biological cells subjected to ultrafast electrical pulses: A numerical simulation study. Physical Review E 62:1025–1033.
[18] Neu, J., K. Smith, and W. Krassowska, 2003. Electrical energy required to form large conducting pores. Bioelectrochemistry 60:107–114.
[19] Sung, W., and P. Park, 1997. Dynamics of pore growth in membranes and membrane stability. Biophysical Journal 73:1797–1804.
[20] Neu, J., and W. Krassowska, 1999. Asymptotic model of electroporation. Physical Review E 59:3471–3482.
[21] Neu, J., and W. Krassowska, 2003. Modeling postshock evolution of large electropores. Physical Review E 67:021915.
[22] Zeng, Y., A. Yip, S. Teo, and K. Chiam, 2012. A three-dimensional random network model of the cytoskeleton and its role in mechanotransduction and nucleus deformation. Biomechanics and modeling in mechanobiology 11:49–59.
[23] Zhang, J., P. Johnson, and A. Popel, 2008. Red blood cell aggregation and dissociation in shear flows simulated by lattice Boltzmann method. Journal of biomechanics 41:47–55.
[24] Zeng, X., and S. Li, 2011. Multiscale modeling and simulation of soft adhesion and contact of stem cells. Journal of the Mechanical Behavior of Biomedical Materials 4:180–189.
[25] Yu, L., Y. Sheng, and A. Chiou, 2013. Three-dimensional light-scattering and deformation of individual biconcave human blood cells in optical tweezers. Optics express 21:12174–12184.
[26] Chee, C., H. Lee, and C. Lu, 2008. Using 3D fluid–structure interaction model to analyse the biomechanical properties of erythrocyte. Physics Letters A 372:1357–1362.
[27] Aernouts, J., I. Couckuyt, K. Crombecq, and J. Dirckx, 2010. Elastic characterization of membranes with a complex shape using point indentation measurements and inverse modelling. International Journal of Engineering Science 48:599–611.
[28] Abidor, I., V. Arakelyan, L. Chernomordik, Y. Chizmadzhev, V. Pastushenko, and M. Tarasevich, 1979. Electric breakdown of bilayer lipid membranes: I. The main experimental facts and their qualitative discussion. Journal of Electroanalytical Chemistry and Interfacial Electrochemistry 104:37–52.
[29] Glaser, R., S. Leikin, L. Chernomordik, V. Pastushenko, and A. Sokirko, 1988. Reversible electrical breakdown of lipid bilayers: formation and evolution of pores. Biochimica et Biophysica Acta (BBA)-Biomembranes 940:275–287.
[30] Barnett, A., 1990. The current-voltage relation of an aqueous pore in a lipid bilayer membrane. Biochimica et Biophysica Acta (BBA)-Biomembranes 1025:10–14.

[31] Deminsky, M., A. Eletskii, A. Kniznik, A. Odinokov, V. Pentkovskii, and B. Potapkin, 2013. Molecular dynamic simulation of transmembrane pore growth. The Journal of membrane biology 246:821–831.
[32] Wohlert, J., W. Otter, O. Edholm, and W. Briels, 2006. Free energy of a trans-membrane pore calculated from atomistic molecular dynamics simulations. The Journal of chemical physics 124:154905.
[33] Taupin, C., M. Dvolaitzky, and C. Sauterey, 1975. Osmotic pressure-induced pores in phospholipid vesicles. Biochemistry 14:4771–4775.
[34] Sugár, I., 1979. A theory of the electric field-induced phase transition of phospholipid bilayers. Biochimica et Biophysica Acta (BBA)-Biomembranes 556:72–85.
[35] Huang, H., F. Chen, and M. Lee, 2004. Molecular mechanism of peptide-induced pores in membranes. Physical review letters 92:198304.
[36] Jean-Franois, F., J. Elezgaray, P. Berson, P.Vacher, and E. Dufourc, 2008. Pore formation induced by an antimicrobial peptide: electrostatic effects. Biophysical Journal 95:5748–5756.
[37] Chernomordik, L., S. Sukharev, S. Popov, V. Pastushenko, A. Sokirko, I. Abidor, and Y. Chizmadzhev, 1987. The electrical breakdown of cell and lipid membranes: the similarity of phenomenologies. Biochimica et Biophysica Acta (BBA) - Biomembranes 902:360 – 373.
[38] Vasilkoski, Z., A. Esser, T. Gowrishankar, and J. Weaver, 2006. Membrane electroporation: the absolute rate equation and nanosecond time scale pore creation. Physical Review E 74:021904.
[39] Li, J., and H. Lin, 2010. The current-voltage relation for electropores with conductivity gradients. Biomicrofluidics 4:013206.
[40] Pastushenko, V., and Y. Chizmadzhev, 1982. Stabilization of conducting pores in BLM by electric current. Gen. Physiol. Biophys 1:43–52.
[41] Weaver, J., 1994. Molecular basis for cell membrane electroporation. Annals of the New York Academy of Sciences 720:141–152.
[42] Newman, J., 1966. Resistance for flow of current to a disk. Journal of the electrochemical society 113:501–502.
[43] Ziebert, F., M. Bazant, and D. Lacoste, 2010. Effective zero-thickness model for a conductive membrane driven by an electric field. Physical Review E 81:031912.
[44] Fletcher, D., and R. Mullins, 2010. Cell mechanics and the cytoskeleton. Nature 463:485–492.
[45] Pravincumar, P., D. Bader, and M. Knight, 2012. Viscoelastic cell mechanics and actin remodelling are dependent on the rate of applied pressure. PloS one 7:e43938.
[46] Kanthou, C., S. Kranjc, G. Sersa, G. Tozer, A. Zupanic, and M. Cemazar, 2006. The endothelial cytoskeleton as a target of electroporation-based therapies. Molecular cancer therapeutics 5:3145–3152.
[47] Teissie, J., and M. Rols, 1994. Manipulation of cell cytoskeleton affects the lifetime of cell membrane electropermeabilization. Annals of the New York Academy of Sciences 720:98–110.
[48] Rols, M., and J. Teissié, 1992. Experimental evidence for the involvement of the cytoskeleton in mammalian cell electropermeabilization. Biochimica et Biophysica Acta (BBA)-Biomembranes 1111:45–50.
[49] Rosazza, C., J. Escoffre, A. Zumbusch, and j. Rols, M. The actin cytoskeleton has an active role in the electrotransfer of plasmid DNA in mammalian cells .
[50] Chang, D., and T. Reese, 1990. Changes in membrane structure induced by electroporation as revealed by rapid-freezing electron microscopy. Biophysical journal 58:1–12.
[51] Wang, H., A. Thiele, and L. Pilon, 2013. Simulations of cyclic voltammetry for electric double layers in asymmetric electrolytes: a generalized modified Poisson-Nernst-Planck model. The Journal of Physical Chemistry C 117:18286–18297.
[52] Kilic, M., M. Bazant, and A. Ajdari, 2007. Steric effects in the dynamics of electrolytes at large applied voltages. II. modified Poisson-Nernst-Planck equations. Physical Review E 75:021503.
[53] Chaudhry, J., J. Comer, A. Aksimentiev, and L. Olson, 2014. A stabilized finite element method for modified Poisson-Nernst-Planck equations to determine ion flow through a nanopore. Communications in computational physics 15.
[54] Olesen, L., M. Bazant, and H. Bruus, 2010. Strongly nonlinear dynamics of electrolytes in large AC voltages. Physical Review E 82:011501.
[55] Zheng, Q., D. Chen, and G. Wei, 2011. Second-order Poisson–Nernst–Planck solver for ion transport. Journal of computational physics 230:5239–5262.
[56] Smith, K., J. Neu, and W. Krassowska, 2004. Model of creation and evolution of stable electropores for DNA delivery. Biophysical Journal 86:2813 – 2826.
[57] Chen, J., M. Abdelgawad, L. Yu, N. Shakiba, W. Chien, Z. Lu, W. Geddie, M. Jewett, and Y. Sun, 2011. Electrodeformation for single cell mechanical characterization. Journal of Micromechanics and Microengineering 21:054012.
[58] Joshi, R., and Q. Hu, 2010. Analysis of cell membrane permeabilization mechanics and pore shape due to ultrashort electrical pulsing. Medical & biological engineering & computing 48:837–844.
[59] Ziebert, F., and D. Lacoste, 2010. A Poisson-Boltzmann approach for a lipid membrane in an electric field. New Journal of Physics 12:095002.
[60] Ambjörnsson, T., M. Lomholt, and P. Hansen, 2007. Applying a potential across a biomembrane: Electrostatic contribution to the bending rigidity and membrane instability. Physical Review E 75:051916.
[61] Dey, M., D. Bandyopadhyay, A. Sharma, S. Qian, and S. Joo, 2012. Electric-field-induced interfacial instabilities of a soft elastic membrane confined between viscous layers. Physical Review E 86:041602.

[62] Vlahovska, R., P.and Gracia, S. Aranda-Espinoza, and R. Dimova, 2009. Electrohydrodynamic model of vesicle deformation in alternating electric fields. Biophysical journal 96:4789–4803.
[63] Seiwert, J., and P. Vlahovska, 2013. Instability of a fluctuating membrane driven by an ac electric field. Physical Review E 87:022713.
[64] Schwalbe, J., P. Vlahovska, and M. Miksis, 2011. Lipid membrane instability driven by capacitive charging. Physics of Fluids 23:041701.
[65] Bingham, R., P. Olmsted, and S. Smye, 2010. Undulation instability in a bilayer lipid membrane due to electric field interaction with lipid dipoles. Physical Review E 81:051909.
[66] Li, J., H. Zhang, F. Qiu, and A. Shi, 2013. Emergence and stability of intermediate open vesicles in disk-to-vesicle transitions. Physical Review E 88:012719.
[67] Li, J., K. Pastor, A. Shi, F. Schmid, and J. Zhou, 2013. Elastic properties and line tension of self-assembled bilayer membranes. Physical Review E 88:012718.
[68] Yao, Z., R. Sknepnek, C. Thomas, and M. Cruz, 2012. Shapes of pored membranes. Soft Matter 8:11613–11619.
[69] Krishna, G., J. Schulte, B. Cornell, R. Pace, L. Wieczorek, and P. Osman, 2001. Tethered bilayer membranes containing ionic reservoirs: the interfacial capacitance. Langmuir 17:4858–4866.
[70] Yin, P., C. Burns, P. Osman, and B. Cornell, 2003. A tethered bilayer sensor containing alamethicin channels and its detection of amiloride based inhibitors. Biosensors and Bioelectronics 18:389 – 397.
[71] Krassowska, W., and P. Filev, 2007. Modeling electroporation in a single cell. Biophysical Journal 92:404 – 417.
[72] Hu, Q., and R. Joshi, 2009. Transmembrane voltage analyses in spheroidal cells in response to an intense ultrashort electrical pulse. Physical Review E 79:011901.
[73] Movahed, S., and D. Li, 2013. A theoretical study of single-cell electroporation in a microchannel. Journal of Membrane Biology 246:151–160.
[74] DeBruin, K., and W. Krassowska, 1999. Modeling electroporation in a single cell. I. effects of field strength and rest potential. Biophysical Journal 77:1213 – 1224.
[75] DeBruin, K., and W. Krassowska, 1999. Modeling electroporation in a single cell. II. effects of ionic concentrations. Biophysical Journal 77:1225 – 1233.
[76] Amestoy, P., I. Duff, J. L'Excellent, and J. Koster, 2001. A Fully Asynchronous Multifrontal Solver Using Distributed Dynamic Scheduling. SIAM Journal on Matrix Analysis and Applications 23:15–41.
[77] Brown, P., A. Hindmarsh, and L. Petzold, 1994. Using Krylov Methods in the Solution of Large-Scale Differential-Algebraic Systems. SIAM Journal on Scientific Computing 15:1467–1488.
[78] Dickens, L., 1967. Spreading Resistance as a Function of Frequency. Microwave Theory and Techniques, IEEE Transactions on 15:101–109.
[79] DeBruin, K., and W. Krassowska, 1998. Electroporation and Shock-Induced Transmembrane Potential in a Cardiac Fiber During Defibrillation Strength Shocks. Annals of Biomedical Engineering 26:584–596.

TABLE S1: Parameter Values for $\mathbf{G_p}$ and $\mathbf{W_{es}}$ Numerical Predictions

Symbol	Definition	Value
$c^{\mathrm{Na}}\|_{t=0}$	Initial Na+ concentration	321.45 mol/m^3
$c^{\mathrm{K}}\|_{t=0}$	Initial K+ concentration	13.39 mol/m^3
$c^{\mathrm{Cl}}\|_{t=0}$	Initial Cl− concentration	334.84 mol/m^3
a_{Na}	Na+ effective ion size	4 Å
a_{K}	K+ effective ion size	5 Å
a_{Cl}	Cl− effective ion size	4 Å
D_w^{Na}	Na+ electrolyte diffusion coefficient in Ω_w	1.33×10^{-9} m^2/s
D_w^{K}	K+ electrolyte diffusion coefficient in Ω_w	1.96×10^{-9} m^2/s
D_w^{Cl}	Cl− electrolyte diffusion coefficient in Ω_w	2.07×10^{-9} m^2/s
ε_w	Electrolyte electrical permittivity	7.083×10^{-10} F/m
ε_m	Membrane electrical permittivity	1.771×10^{-11} F/m
F	Faraday constant	9.6485×10^4 C/mol
C_s	Stern layer capacitance	1 pF
k_B	Boltzmann constant	$1.3806488 \times 10^{-23}$ J/K
T	Temperature	300 K
ϕ_e	Electrode potential	100-500 mV
ϕ_{ec}	Counter electrode potential	0 mV
l_r	Tether reservoir length	400 nm
h_r	Tether reservoir height	4 nm
h_m	Membrane thickness	4 nm
h_e	Electrolyte height	60 nm

TABLE S2: Parameter Values for Current Predictions

Symbol	Definition		Value		
γ	Edge energy		1.8×10^{-11} J/m		
σ	Surface tension		1×10^{-3} J/m^2		
C	Steric repulsion constant		9.67×10^{-15} J$^{1/4}$ m		
D	Radial diffusion coefficient		1×10^{-14} m^2/s		
α	Creation rate coefficient		1 Gs^{-1} $\left[10\ \text{Ms}^{-1} - 0.1\ \text{Ts}^{-1}\right]$		
q	$q = (r_m/r_*)^2$ with the symbols defined below Eq. 17		2.46±0.07		
DphPC Membrane		**Tether Density:**	**1%**	**10%**	**100%**
G_0	Initial membrane conductance		1.67±0.3 μS	0.91±0.04 μS	0.43±0.03 μS
C_m	Membrane capacitance		10.5±0.8 nF	10.5±0.7 nF	11.0±0.2 nF
R_e	Electrolyte resistance		3.5±1 kΩ	3.5±1 kΩ	5.0±2.0 kΩ
C_{dl}	Total electrode double-layer capacitance		136.3±6 nF	136.3±8 nF	118.2±8 nF
V_{ep}	Characteristic voltage of electroporation		430±5 mV	430±5 mV	580±10 mV
N_o	Equilibrium pore density		1068 [120-15k]	582 [90-10k]	275 [42-43k]
K_t	Spring constant		0 N/m	2±0.5 mN/m	20±5 mN/m
DphPC Membrane (Reservoir Double-Layer Effect)		**Tether Density:**	**1%**	**10%**	
G_0	Initial membrane conductance		1.00±0.1 μS	1.00±0.1 μS	
C_m	Membrane capacitance		14.6±0.1 nF	16.0±0.4 nF	
R_e	Electrolyte resistance		1.0±0.5 kΩ	1.0±0.5 kΩ	
C_{dl}	Total electrode double-layer capacitance		65±3 nF	39±2 nF	
V_{ep}	Characteristic voltage of electroporation		366±6 mV	400±5 mV	
N_o	Equilibrium pore density		641 [100-2k]	641 [100-50k]	
K_t	Spring constant		0 N/m	2±0.5 mN/m	